

Structural Multi-Colour Invisible Inks with Submicron 4D Printing of Shape Memory Polymers

Wang Zhang¹, Hao Wang^{1*}, Hongtao Wang¹, John You En Chan¹, Hailong Liu^{1,2}, Biao Zhang³, Yuan-Fang Zhang⁴, Komal Agarwal¹, Xiaolong Yang⁵, Hong Yee Low¹, Qi Ge⁶, Joel K.W. Yang^{1,2*}

¹Engineering Product Development, Singapore University of Technology and Design, Singapore 487372, Singapore. ²Nanofabrication Department, Institute of Materials Research and Engineering, Singapore 138634, Singapore. ³Frontiers Science Center for Flexible Electronics, Xi'an Institute of Flexible Electronics (IFE) and Xi'an Institute of Biomedical Materials & Engineering (IBME), Northwestern Polytechnical University, 127 West Youyi Road, Xi'an 710072, China. ⁴Digital Manufacturing and Design Centre, Singapore University of Technology and Design, Singapore 487372, Singapore. ⁵National Key Laboratory of Science and Technology on Helicopter Transmission, Nanjing University of Aeronautics and Astronautics, Nanjing 210016, China. ⁶Department of Mechanical and Energy Engineering, Southern University of Science and Technology, Shenzhen 518055, China.

*email: hao_wang@sutd.edu.sg; joel_yang@sutd.edu.sg

Abstract

Four-dimensional (4D) printing of shape memory polymer (SMP) imparts time responsive properties to 3D structures. Here, we explore 4D printing of a SMP in the submicron length scale, extending its applications to nanophononics. We report a new SMP photoresist based on Vero Clear achieving print features at a resolution of ~300 nm half pitch using two-photon polymerization lithography (TPL). Prints consisting of grids with size-tunable multi-colours enabled the study of shape memory effects to achieve large visual shifts through nanoscale structure deformation. As the nanostructures are flattened, the colours and printed information become invisible. Remarkably, the shape memory effect recovers the original surface morphology of the nanostructures along with its structural colour within seconds of heating above its glass transition temperature. The high-resolution printing and excellent reversibility in both microtopography and optical properties promises a platform for temperature-sensitive labels, information hiding for anti-counterfeiting, and tunable photonic devices.

Keywords: 4D printing, two-photon polymerization lithography, shape memory polymer, programmable colour generation

Introduction

4D printing¹⁻³ brings together the design flexibility of 3D printing with stimuli responsive properties of its constituent materials. It continues to generate excitement in diverse fields, e.g., soft robotics⁴⁻⁶, drug delivery^{7,8}, flexible electronics^{9,10} and tissue engineering¹¹. Commonly used printing methods for 4D printing include direct ink writing^{3,12}, Polyjet^{13,14}, Digital Light Processing (DLP) lithography^{15,16} and Stereolithography (SLA)^{17,18}. The material and lithographic challenges inherent to these methods limit the minimum feature size of printed structures to $\sim 10\ \mu\text{m}$.¹⁹ At an order of magnitude smaller, submicron scale features that interact strongly with light have yet to be systematically explored in 4D printing.

The motivation to improve print resolution is fuelled by applications in optics, e.g. structural colour generation^{20,21}, temperature sensitive passive labels, and colorimetric pressure sensors, all of which require submicron resolution and precision. Traditionally, different structures such as gratings^{22,23}, thin films and multilayers^{24,25}, localized resonance structures^{26,27} generate fixed colours without the use of pigments. Recently, dynamically reconfigurable colours have gained interest, where optical responses of nanostructures can be tuned either by changing the refractive index²⁸⁻³⁰ or dimensions^{31,32} of the structures. Of these methods, tuning the dimensions of the optical devices by shape memory polymers (SMPs) is of interest due to their relatively short response times (seconds to minutes depending on actuation temperature³³). Distinct from the patterning of SMPs through nanoimprinting³⁴⁻³⁶ and self-assembly³⁷⁻³⁹, our use of 3D printing introduced here will lead to direct patterning of complex structures at will, bringing together fields of mechanical and optical metamaterials with local control of properties, e.g., colours⁴⁰, phase, and Young's modulus.

To print finer 3D structures, we develop a new resist suited for two-photon polymerization lithography (TPL)^{6,41,42}. Here, photo-initiators in a liquid resin are excited by a two-photon absorption process within the focal region of a femtosecond laser. Polymerization and crosslinking then ensue. Printed features as small as $\sim 10\ \text{nm}$ can be achieved under specific conditions.⁴³ Due to the high resolution it provides, TPL has been used to print different stimuli responsive materials such as hydrogels^{6,44}, liquid crystal elastomers^{41,45}, magnetic nanoparticles embedded resists^{46,47}, silicon functionalized monomers⁴⁸, and other examples printing⁴⁹. Recently, hydrogel photoresists have been used for tunable photonic devices. Marc et al.⁵⁰ used a cholesteric liquid crystals (LC)-based hydrogel resist to change colours at microscale. In their work, colours were tuned within a limited range by changing the intrinsic periodicity of chiral LC. Tao et al.⁵¹ demonstrated a hydrogel based reconfigurable photonic

crystals exhibiting colour shifts in the presence of humidity. In contrast to previous works reporting colour shifts, our work investigates submicron 4D printing where large and rapid visual responses are achieved as nanostructures recover from a flattened (colourless) state to an upright (colourful) state. The visual effect is analogous to a letter written in multiple colours of invisible ink where secret information is revealed, e.g., with the application of heat. We tackled two key challenges in (1) developing and characterizing new stimuli responsive resists suitable for TPL, and (2) designing and fabricating robust 3D photonic structures capable of rapid recovery after being flattened.

In this work, we meet these challenges by additive manufacturing of SMP for programmable colour generation. We developed and characterized a SMP photoresist suited for TPL based on Vero Clear¹³, which is an optically transparent thermosetting polymer resin containing acrylate functional group. We performed resolution tests achieving ~300 nm half pitch gratings and measured the thermodynamic properties of the new resist to determine an optimal composition for robust mechanical performance. A range of structural colours were achieved by controlling the geometry of the crosslinked SMP structures at the submicron level. We realized colour switching behaviour by heating and deforming (i.e. programming) the printed structure at 80 °C. Remarkably, the deformed nanostructures exhibited excellent recovery when heated above its composition-adjustable glass transition temperature (T_g). This reversibility in both structural features and optical responses demonstrate significant promise for submicron scale additive manufacturing of SMPs.

Results

Two-photon polymerization lithography of shape memory polymer

We designed structures consisting of a base layer with submicron-scale grids on top of it, as shown in Figure 1. Due to the interaction of these nanostructures with light, i.e., scattering and interference, the 3D printed structures function as colour filters, preferentially transmitting certain wavelength ranges of an incident white light illumination. Colours depend sensitively on the geometric parameters of the grid, i.e., grid height h_2 , and grid linewidth w_1 , while it is less sensitive to pitch w_2 and the thickness of the base layer h_1 . By printing in SMP, we realize a 4D effect, with the ability to change its geometry and optical properties in response to temperature variation as a function of time.

To achieve the shape memory effect, the print is first deformed at a temperature T_h higher than the SMP's glass transition temperature. While keeping the external load, the temperature is decreased to $T_l (< T_g)$ as the print transitions from a soft rubbery state to a stiff

glassy state. Here, in the altered flattened geometry the print loses its colour, rendering the print “invisible”. The temporary configuration is achieved at T_l after releasing the external load as the polymer chains are “frozen” at its glass state. The print finally recovers to its original geometry and colour when heated back to T_h where the polymer chains regain the entropic elasticity.

A Vero Clear¹⁴ based SMP photoresist was developed (See Methods and Figure S1 for the preparation process). To test the resist, we placed a droplet of it onto a fused silica glass substrate and exposed using in the commercial TPL system Nanoscribe GmbH Photonic Professional GT using the “dip-in” configuration^{40,52,53}. During exposure, photo-initiators at the focal point of the objective are activated by two-photon excitation from the femtosecond pulsed laser at 780 nm wavelength, leading to polymerization of the resist into solid structures. After exposure, the uncured resist was removed using a development process (see Methods for details). The characterization of the photoresist is provided in Supplementary part 2. With the characterized resist, we were able to print samples with linewidth of ~ 280 nm (Figure S2e) and conservative minimum resolvable pitch of 600 nm (i.e. 300 nm half pitch, Figure S2f). To the best of our knowledge, these are the smallest feature sizes and highest print resolutions achieved via additive manufacturing of a SMP.

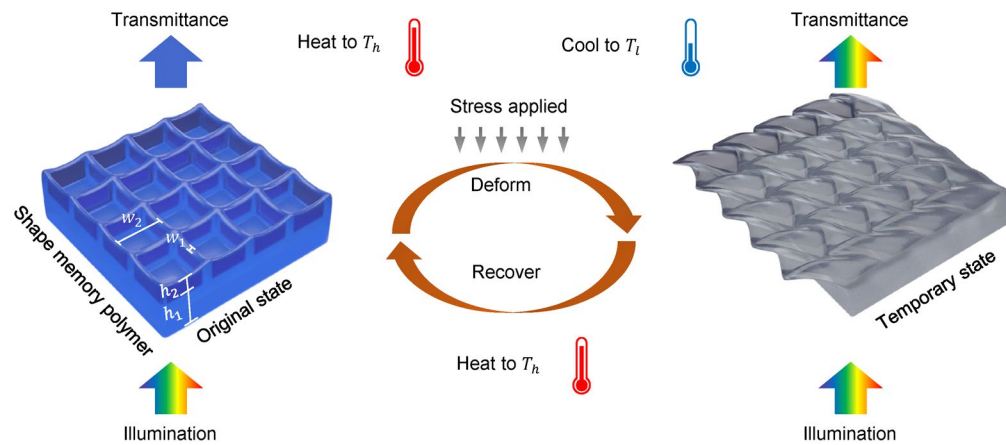


Figure 1. Schematic of colour and shape change of a constituent nanostructured element of the “invisible ink” 3D printed in shape memory polymer (SMP). The as-printed structures with upright grids (left) function as a structural colour filter that transmits only a limited wavelength range of visible light. Deformation of the structures at elevated temperature flattens the nanostructures (right) rendering it colorless, where it remains in an invisible state after cooling to room temperature. Heating recovers both the original geometry and color of nanostructures, leading to a submicron demonstration of 4D printing.

Characterization of colours

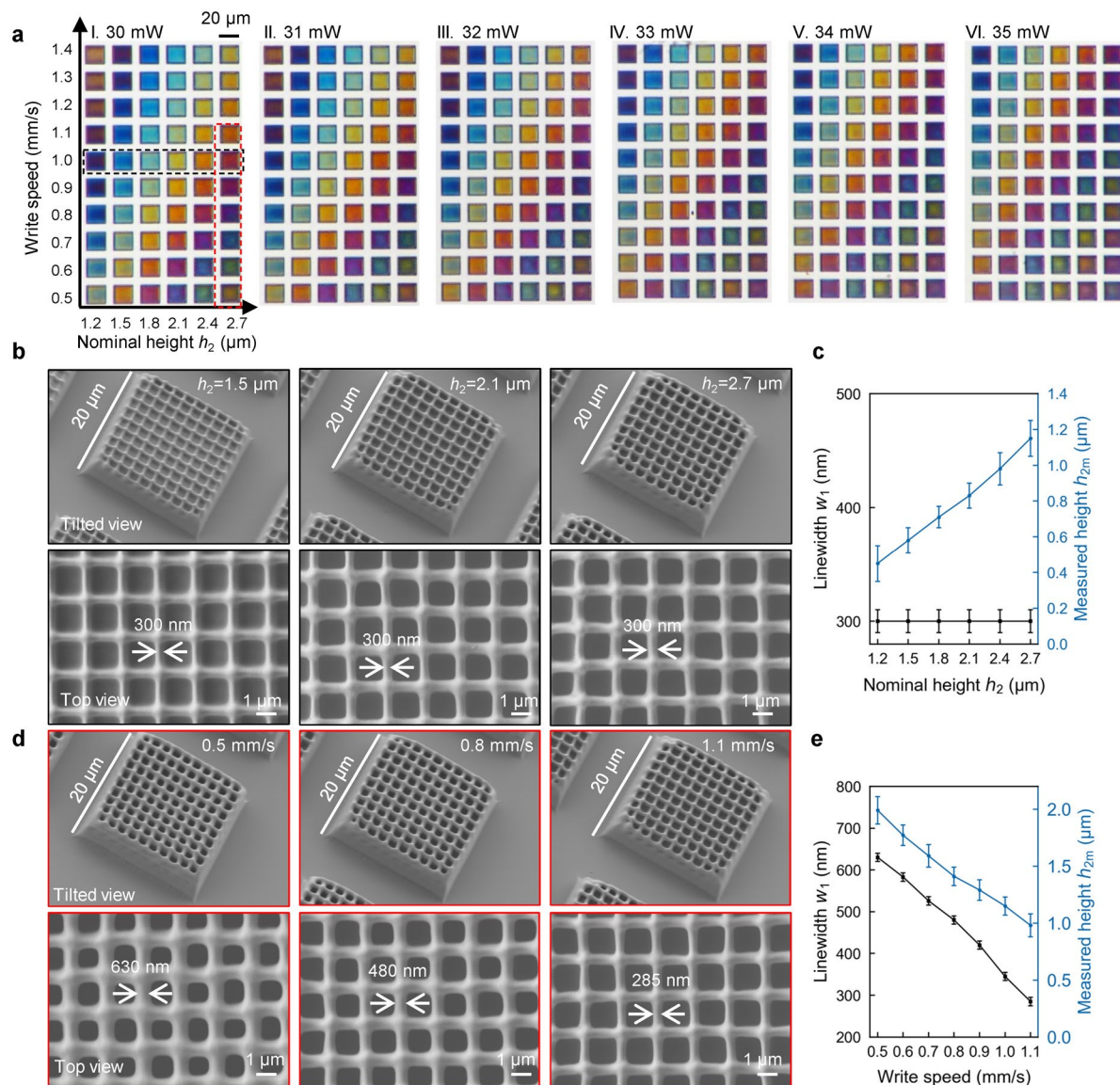


Figure 2. Optical and scanning electron micrographs of as-printed structures. (a) Optical transmittance micrographs of a printed colour palette for a constant pitch of 2 μm but varying write speed and nominal height h_2 for a range of laser power (I-VI laser power 30-35 mW respectively); (b) SEM images of grid structures with different nominal height h_2 for constant write speed of 1 mm/s and laser power of 30 mW; (c) Measured grid linewidth and height as a function of nominal height; (d) SEM images for grid structure with different write speeds for fixed nominal height of 2.7 μm and laser power of 30 mW; (e) Measured grid linewidth and height as a function of write speed.

We next investigate the different colours achieved by the grid structure shown in Figure 1 and how it depends on the various design parameters. As h_1 only affects the phase of light and does not contribute to the change of colour, it is fixed at $\sim 4 \mu\text{m}$ to raise the grids above the substrate making it easier to compress. The two parameters h_2 and w_1 can be varied by controlling the write speed, laser power and number of grid layers. Figure 2a shows a

transmittance optical micrograph of a colour palette as a function of write speed w_1 and nominal height h_2 for a range of laser power (30-35 mW) and fixed pitch w_2 (see Table S1 for the fabrication parameters). The corresponding transmittance spectra for Figure 2aI were measured using a CRAIC microspectrophotometer and mapped onto the CIE 1931 chromaticity diagram in Figure S3, demonstrating a reasonably wide range of colours. To study the effect of pitch w_2 on colour, we fabricated structures of constant nominal height h_2 of 1.8 μm and varied its pitch. The transmittance spectra for structures with different pitches are shown Figure S4a (see the corresponding SEM images in Figure S4b-h). When w_2 is 1 μm , the adjacent lines are fused together during the polymerization process, and produce a nearly transparent patch. When w_2 is 3 μm , the gaps are too wide, leading to low colour saturation. Thus, a gap of 2 μm was chosen for the remainder of our studies. Here the minimum resolvable pitch w_2 is larger than that in Figure S2f, which could be caused by the proximity effect while printing multilayer grids. It should be noted that the experimental obtained colour gamut in Figure 2a can be further extended by decreasing the pitch w_2 to increase the colour saturation.

Figure 2b shows representative SEM images for grids with different nominal heights at a fixed write speed of 1 mm/s and laser power of 30 mW (black rectangle in Figure 2a). Generally, the central region of the grid remains stable with increasing height of the grid, while the corners start to collapse due to resist shrinkage and lack of support structures. The collapsed structures account for nonuniformity in colour at the edges of the square patches in Figure 2a. As both the laser power and write speed were kept constant, the linewidth of the grid does not change with increasing nominal height as shown in the top view SEM images in Figure 2b. Both the linewidth w_1 and height h_2 for the grid structure in the black box are plotted in Figure 2c. The height increases at an interval of 100 nm per layer, which is less than the nominal layer height (300nm as shown in Table S1) as a result of shrinkage during the writing and development (rinsing) process.

To study the influence of write speed on the structure, Figure 2d shows representative SEMs for structures with different write speeds and constant nominal height inside the red box in Figure 2a and the measured dimensions are summarized in Figure 2e. The linewidth decreases from 630 nm to 285 nm as the increase of write speed from 0.5 mm/s to 1.1 mm/s, while the height of the grid decreases from 1990 nm to 980 nm. Figure S5 shows the SEM images and measured dimensions for structures with different laser power in Figure 2a. The effect of write speed and laser power on the structure size can be attributed to the roughly relation *curing spot size* \sim *laser power*²/*write speed*. With increasing write speed and decreasing

laser power, the energy received per unit area decreases, leading to less polymerization and an effectively smaller curing spot size, resulting in a narrower linewidth and shorter structures.

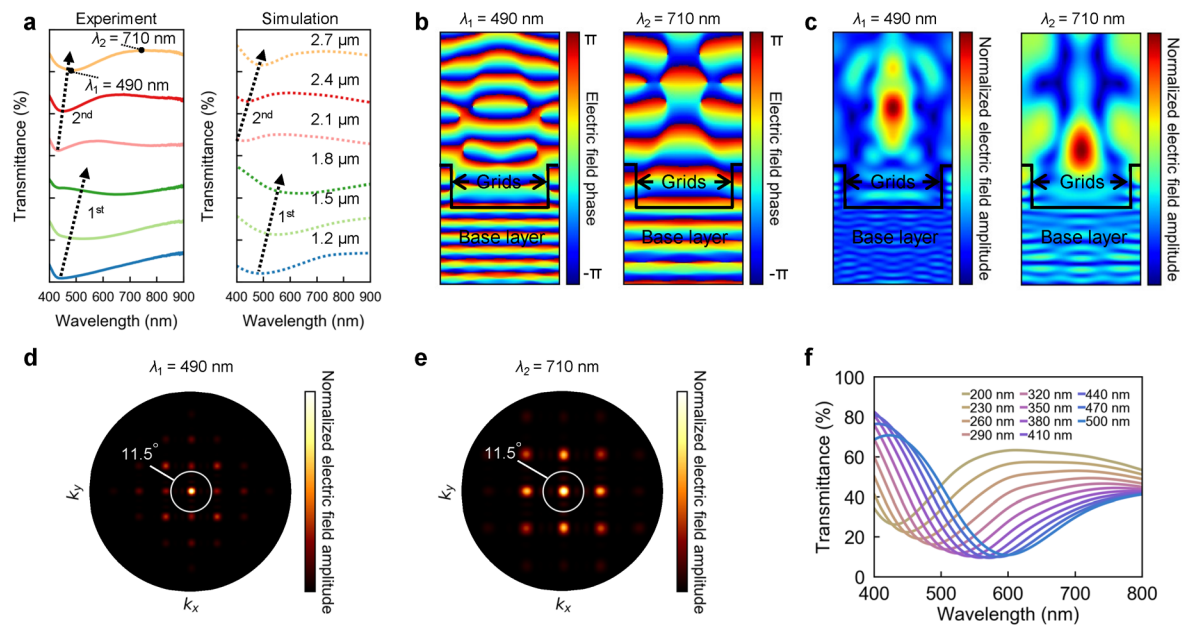


Figure 3. Finite Difference Time Domain (FDTD) analysis of the grid structure (a) Measured and FDTD simulated transmittance spectra of structures with different nominal height h_2 (from the black dashed rectangle in Figure 3a ranging from 1.2 μm to 2.7 μm). Marked positions $\lambda_1=490$ nm and $\lambda_2=710$ nm are used for FDTD field analysis in Figure 3b-e; (b)-(c) Cross section view of near field normalized electric field phase and amplitude for a grid structure (laser power:30 mW, write speed: 1mm/s, nominal grid height: $h_2=2.7$ μm) at dip transmittance 490 nm and peak transmittance 710 nm wavelength respectively; (d)-(e) Top view of far field normalized electric field amplitude for the above grid structure at dip transmittance 490 nm and peak transmittance 710 nm wavelength respectively; the white circle represents collection field for the microscope used in this work (NA=0.2, CA=11.5 $^\circ$); (f) Simulated transmittance spectra for structures with different linewidth w_1 (the colours of the spectrum lines were mapped from the corresponding spectra).

Though we have previously reported high aspect ratio pillars as colour generating structures^{53,54}, this is the first time that we are experimenting with grid structures. The grid structures provide greater mechanical stability needed in this study. To gain some understanding of the colour generating nature of this design, we measured the transmittance spectra of the grid structures inside the black box and performed Finite Difference Time Domain (FDTD) simulations to obtain the spectra (Figure 3a). A comparison of the measured and simulated data is provided in Figure S7. The simulation results show a good qualitative agreement with the experiment. The discrepancies could arise from the idealized structures used in the simulations that do not account for rounded edges. A redshift effect of the spectrum position is observed in Figure 3a and shown by the dotted arrows. The simulated near field

electric field phase and amplitude for one structure (fabricated with the laser power of 30 mW, write speed of 1 mm, nominal grid height of 2.7 μm) at wavelength of 490 nm and 710 nm (corresponding to the marked dip and peak of the spectrum in Figure 3a) are shown in Figure 3b and c, respectively. The incident plane wave passes through the base layer without scattering. After propagating through the submicron grids, the wave front is delayed compared to the wave fronts that pass through the air gap. As seen in the near field phase plot in Figure 3b, the regions within and directly above the grid lines appear to accumulate phase faster than the region in between. The interference of these two regions of transmitted light causes some focusing and redistribution of the energy flow of light (see corresponding electric field amplitude of the near field in Figure 3c). For the peak and dip positions, the constructive interferences occur at different parts above the structure. The far field energy distribution can be obtained by performing the near-field-to-far-field transform. Figure 3d and e present the normalized far field electric field amplitude within the objective collection angle (CA) for the dip and peak position respectively, corresponding to experimental observation with objective lens adopted in our experiment (the NA=0.2, CA=11.5°). The integration of the far field electric intensity within the collection angle results in the transmittance spectra dip and peak shown in Figure 3a.

As discussed in Figure 2, write speed and laser power affect both linewidth w_1 and grid height h_2 . To study the influence of w_1 alone on colour, we simulated the spectra for a fixed height h_2 of 0.9 μm and varied the linewidth w_1 (Figure 3f). As the linewidth increases from 200 nm to 500 nm, the transmittance dip redshifts from 450 nm to 600 nm, resulting a shift of the transmitted colour from yellow to blue. This effect could be risen from the increase of effective refractive index as the increase of w_1 . See Supplementary Information part 9 for a detailed discussion about this relation. The redshift effect of the measured spectra as the increasing of laser power and decreasing of write speed in Figure S8c could be explained by the increase of effective refractive index. This result suggests that one could also achieve large colour variation simply by varying the width of the structures.

Submicron scale shape memory effect

To study the shape memory effect of the submicron scale structure, we printed a colour palette (Figure 4aI), with a fixed nominal height of 1.8 μm , but varied the laser power and write speed from 30 mW to 35 mW horizontally with a step of 0.5 mW and 0.6 mm/s to 1.1 mm/s vertically with a step of 0.05 mm/s respectively. Doing so also generates a broad range of colours due to variation in both width and height of the structures. The structures were then heated above its

T_g to 80 °C using a heat gun. Under the high temperature, a stress of ~500 kPa was applied using a metal block on the surface of the structure. Then the sample was cooled down to room temperature in air (in ~30 seconds) with the metal block maintained. Upon removal of the load, the deformed structures appear transparent as shown in Figure 4aII. All the colours were recovered when the sample was heated up again to 80 °C by the heat gun (Figure 4aIII). The recovery process occurs within seconds due to the rapid response of the SMP. The detailed setup of this programming process is provided in Figure S9. We compared the spectra of three different colours (marked as 1-3 in Figure 4a) before and after the programming and recovery processes, shown in Figure 4b. The spectra of the original and recovered colours are almost identical except for a small but systematic blueshift, indicating a good recoverability of our 4D printing. The compressed structure exhibited high transmittance ~80% across the visible spectrum, leading to a transparent appearance devoid of colour.

SEM images (Figure 4c) of structure 2 were taken at the three states (as printed, after compression, and after recovery) showing the change in nanostructure geometry and revealing the underlying mechanism of colour variation. The original grids appear as regular squares, with light scattering and colour generating properties, as explained above. However, the compressed structures appear as irregular quadrangles, with the pits in grid completely closed up due to buckling and collapsing of the walls of the grid into a fish-scale pattern. This configuration is expected to result in weak scattering in the visible spectrum, due to the reduced height of the structures and lack of clear structure definition.

As the structures have been squeezed to the point of contact between surfaces, one would have predicted that this deformation was irreversible. Experience with collapsed nanostructures from capillary forces teaches us that the stiction Van der Waals forces will keep these nanostructures together⁵⁵. Yet, once heated above T_g again, the grids recover to regular squares again due to the shape memory effect. The top view of structure 2 during the programming process is given in Figure 4c, in which the linewidth before deformation and after recovery matches well, indicating a good shape recovery effect. It should be noted that as there was no support on the edges of grids, the walls along the edge might have been too thin to overcome the stiction forces and could not recover, as shown in the tilted view SEM image in Figure 4cIII. This irreversible damage account for some of the dark corners and edges of the recovered structures in Figure 4aIII.

To further understand the programming process, Figure 4d shows spectra for a structure programmed into different degree of flatness, and the corresponding SEM images are given in

Figure 4e. When the structure is slightly flattened (Figure 4eII), the grids configuration is similar to the original one (Figure 4eI), and there are only gentle shifts of both colour and spectrum (Figure 4d). While the structure is further flattened, the gaps between the grids are filled (Figure 4eIII-IV), leading to high transmittance of light wavelength in the whole visible range and a transparent appearance (Figure 4d). The robustness of the programming process is checked in Figure 4f by programming a structure for 4 times, the spectra for recovered structures in different cycles match well, indicating a good repeatability of the shape memory effect.

To demonstrate the potential application, we printed an image of an art piece by one of the authors, depicting an octopus in foreground with a mountainous landscape in the background (Figure 4gI). This image comprised 52×52 pixels with each pixel designed as $10 \mu\text{m}$. The print was then programmed into a transparent featureless image as shown in Figure 4gII, using the same process. Here both the octopus and its surrounding have become invisible. Upon heating, the painting recovers to its original state again as shown in Figure 4gIII. Figure S10 presents the SEM images of the top left corner of the original painting. In Figure S10a, different parts were printed by different nominal heights, resulting in different colours in Figure 4g. To make the whole structure stable, the lines along two adjacent write fields were written twice, leading to wider lines comparing to lines within one write field as shown in Figure S10b. And the grids near the boundaries are stretched to be wider, which results in slightly different colour along the boundaries of different write fields. To overcome this issue, some more stable photoresist with higher stiffness and less shrinkage should be developed in the future.

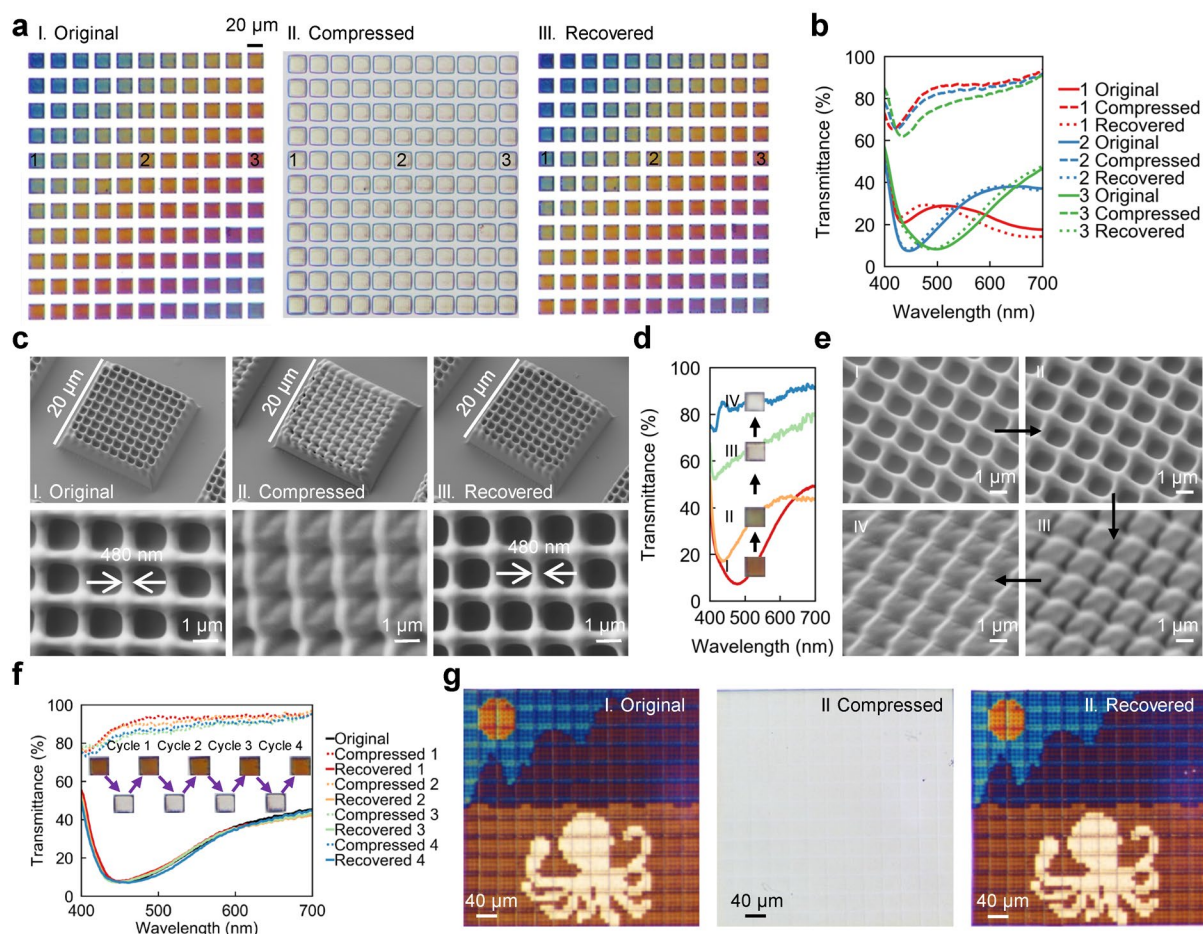


Figure 4. Submicron scale shape memory effect (a) Different colours as printed, compressed and recovered respectively, observed by the objective lens (NA=0.2, CA=11.5°) at the transmittance mode (In the colour palette, the laser power was varying from 30 to 35 mW with a step of 0.5 mW in the transverse direction, and the write speed was varying from 0.6 to 1.1 mm/s with a step of 0.05 mm/s in the vertical direction); (b) Comparison of measured spectra of three different grid structures (marked as number 1, 2, 3 in Figure 4a) as printed, after programming and after recovery; (c) Tilted (30° tilt angle) and top view of SEM images before and after programming and after recovery; (d) Measured spectra and (e) SEM images for a structure programmed into different degree of flatness; (f) Measured spectra of a grid structure for 4 programming cycles. (g) The painting as printed, compressed and recovered, respectively.

Discussion

By fabricating of the characterized SMP photoresist, we printed 300 nm scale structures with good recoverability in both microtopography and optical properties. There is still room for improvement of resolution comparing to commercially available photoresist such as IP-Dip (~100 nm feature size^{56,57}). An ideal SMP for TPL should have high stiffness at the glassy state and low shrinkage during printing to avoid collapse and distortion so as to further bring down the feature size. Meanwhile it should have good stretchability at the rubbery state to avoid irreversible break during programming. Also, micron and submicron scale mechanical test

should be implemented to understand the micromechanical behaviour of the printing. These issues should be investigated in the future works.

In conclusion, we demonstrated the concept of submicron scale 4D printing of shape memory polymer with the application for multi-colour invisible inks by two-photon polymerization lithography of the custom-tailored photoresist. Due to the flexible tunability of the design variables by additive manufacturing, different colours can be easily obtained by varying the printing parameters such as laser power, write speed and nominal height of grids. The printed structures can switch colour stably and rapidly by the programming process. Though there are some key challenges in this area, we believe that this approach opens up potential applications of 4D printing in high precision required fields such as optics and sensors.

Methods

Preparation of photoresist

0.9 g of 2-hydroxy-3-phenoxypropyl acrylate (HPPA) and 0.1 g of Bisphenol A ethoxylate dimethacrylate (BPA) were mixed together and stirred by a vibration generator system for 5 mins to get homogeneous solution. 20 mg of diphenyl (2,4,6-trimethylbenzoyl) phosphine oxide (TPO) was added to this solution and stirred by a magnetic rotor for 1 h to get the elastomer resist. The elastomer resist was mixed with Vero Clear at different mass fractions and stirred for 5 mins to get the SMP photoresist. The photoresist was kept in brown glass bottle at 22 °C to avoid polymerization before printing. Vero Clear was purchased from Stratasys, while HPPA, BPA and TPO were purchased from Sigma-Aldrich. The chemicals were used as received.

Two-photon polymerization lithography

Before writing, a fused silica substrate ($25 \times 25 \times 0.7$ mm³, refractive index = 1.46) was cleaned with IPA solution in ultrasound for 2 mins. The substrate was baked at 120 °C for 10 mins on a hotplate, then cooled to room temperature. Then the substrate was spin-coated with TI PRIME adhesion promoter (MicroChemicals GmbH, Germany) at 2000 rpm for 20 s. The substrate was again baked at 120 °C for 2 mins on a hotplate, then cooled to room temperature. A drop of photoresist was placed onto the coated side of the substrate, then the substrate was transferred to a two-photon lithography system (Photonic Professional GT, Nanoscribe GmbH, Germany). A 63×NA1.4 oil immersion objective lens in Dip-in Laser Lithography (DiLL) configuration was used. The laser power and write speed were set to 30-40 mW and 0.5-2 mm/s, respectively. After writing, the substrate was immersed in propylene glycol monomethyl ether acetate (PGMEA) for 5 mins, isopropyl alcohol (IPA) for 2 mins and deionized water for 1

min to remove the uncured resist. The substrate was blown with a N₂ gun to remove the water, then cured with UV exposure of 365nm and ~1 J/cm² for 10 mins (UVP® CL-1000® Ultraviolet Crosslinkers, USA). Finally, the substrate was kept in a clean container for 2 days to release residual stress.

Materials characterization

The dynamic mechanical analysis tests were conducted on a DMA tester (TA Instruments, Q800 DMA, U.S.) in the tension film mode. After erasing thermal history at 80 °C for 5 min, DMA tests started from 80 to 0 °C at a cooling rate of 3 °C/min. For the test of pure elastomer, the test was started at 40 °C to avoid rupture. The dimensions of the testing samples were 6 mm × 15 mm × 0.5 mm and was prepared by curing the photoresist in a Teflon mould in the UV oven with a power of ~1 J/cm² for 10 mins.

The uniaxial tensile experiments were conducted on the DMA tester (TA Instruments, Q800 DMA, U.S.). The samples were prepared by the same method as above. The test was conducted using the stress control mode with a stress rate of 2 MPa/min. The temperature was controlled to be 20 °C higher than the glass transition temperature (T_g) for each composition.

The viscosity tests were conducted on a Discovery Hybrid Rheometer (DHR2, TA instruments Inc., UK) with an aluminium plate geometry (20 mm in diameter), with frequency ranging from 10 to 4000 Hz. The temperature was precisely controlled to be 22 °C by a Peltier system. The plate gap was set as 100 μm.

The SEM images was taken with a JSM-7600F Schottky Field Emission Scanning Electron Microscope (JEOL, Japan) using a voltage of 5kV. Before the test, the samples were sputtered with gold in vacuum for 60 seconds with a current of 40 mA at the control gas manual mode.

The height of the structures was measured by a Profilometer KLA Tencor D-600 (KLA Inc., U.S.). The scan speed was 0.01mm/s and the stylus force was 1 mg.

The refractive index of the photoresist needed for FDTD simulation was measured by an EP4 Ellipsometer (ACCURION, Germany). A wafer substrate was cleaned with IPA and then baked on a hotplate at 130 °C for 10 mins. Then the resist was spin coated on the substrate with a speed of 7000 rpm for 1 min. Then the substate was baked again on the hotplate 130 °C for 3 mins. Afterwards, the sample was used for the measurement of the ellipsometry angles Δ and Ψ of the photoresist. The refractive index n and extinction coefficient k were fitted based on the measured Δ and Ψ using the Cauchy dispersion function as shown in Supplementary information Part 7.

Optical measurements

Transmittance spectra were measured using an objective lens (NA=0.2, CA=11.5°) on an optical microscope (Nikon Eclipse LV100ND) with a CRAIC 508 PV microspectrophotometer and a Nikon DS-Ri2 camera. Samples were illuminated with a halogen lamp. The spectra (transmittance mode) are normalized to the transmittance spectrum of fused silica glass, which is measured under the same conditions as for the sample.

Numerical Simulation

FDTD simulation to calculate the theoretical spectra was conducted with a commercial software (FDTD, Lumerical Solutions). The dimension profile for the simulation was obtained from the SEM images and the Profilometer. In FDTD simulation, planewave was injected from bottom of grids and base layer, then electric field and corresponding power components were collected and followed by a near-to-far-field transform process. The final spectra were obtained by integration of the energy within the collecting angle of the objective lens used in measurement.

Data availability

All data are available from the corresponding author upon reasonable request.

Acknowledgements

J.K.W.Y. acknowledges funding support from the National Research Foundation (NRF) Singapore, under its Competitive Research Programme award NRF-CRP20-2017-0004, SUTD Digital Manufacturing and Design (DManD) Center grant RGDM1830303, and THALES-SUTD project RGTHALES1901. B.Z. acknowledges the National Natural Science Foundation of China (No. 51903210), Natural Science Basic Research Program of Shanxi (Program No. 2020JQ-174), the Fundamental Research Funds for the Central Universities (No. 31020190QD015).

Author Contributions

W.Z. conceived the idea, designed the experiments, characterized the photoresists, and fabricated the samples with the assistance from H.W. H.T.W. performed the FDTD simulation. J.Y.E.C., H.L.L., B.Z., Y.F.Z., K.A., X.L.Y. assisted the fabrication and characterization. J.K.W.Y. supervised the research in discussion with H.Y.L. and Q.G. All authors contributed to writing and revision of the manuscript.

Competing interests

The authors declare no competing interests.

Additional information

Supplementary Information is available for this paper.

References

- 1 Ge, Q., Qi, H. J. & Dunn, M. L. Active materials by four-dimension printing. *Appl. Phys. Lett.* **103**, 131901 (2013).
- 2 Ge, Q., Dunn, C. K., Qi, H. J. & Dunn, M. L. Active origami by 4D printing. *Smart Mater. Struct.* **23**, 094007 (2014).
- 3 Gladman, A. S., Matsumoto, E. A., Nuzzo, R. G., Mahadevan, L. & Lewis, J. A. Biomimetic 4D printing. *Nat. Mater* **15**, 413 (2016).
- 4 Truby, R. L. & Lewis, J. A. Printing soft matter in three dimensions. *Nature* **540**, 371 (2016).
- 5 Zhang, Y. F. *et al.* Fast-Response, Stiffness-Tunable Soft Actuator by Hybrid Multimaterial 3D Printing. *Adv. Funct. Mater.* **29**, 1806698 (2019).
- 6 Hippler, M. *et al.* Controlling the shape of 3D microstructures by temperature and light. *Nat. Commun.* **10**, 232 (2019).
- 7 Malachowski, K. *et al.* Stimuli-responsive theragrippers for chemomechanical controlled release. *Angew. Chem. Int. Ed.* **53**, 8045-8049 (2014).
- 8 Breger, J. C. *et al.* Self-folding thermo-magnetically responsive soft microgrippers. *ACS Appl. Mater. Interfaces* **7**, 3398-3405 (2015).
- 9 Zarek, M. *et al.* 3D printing of shape memory polymers for flexible electronic devices. *Adv. Mater.* **28**, 4449-4454 (2016).
- 10 Su, J.-W. *et al.* 4D printing of a self-morphing polymer driven by a swellable guest medium. *Soft Matter* **14**, 765-772 (2018).
- 11 Kuribayashi-Shigetomi, K., Onoe, H. & Takeuchi, S. Cell origami: self-folding of three-dimensional cell-laden microstructures driven by cell traction force. *PLOS ONE* **7**, e51085 (2012).
- 12 Kuang, X. *et al.* 3D printing of highly stretchable, shape-memory, and self-healing elastomer toward novel 4D printing. *ACS Appl. Mater. Interfaces* **10**, 7381-7388 (2018).
- 13 Mao, Y. *et al.* Sequential self-folding structures by 3D printed digital shape memory polymers. *Sci. Rep.* **5**, 13616 (2015).
- 14 Ding, Z. *et al.* Direct 4D printing via active composite materials. *Sci. Adv.* **3**, e1602890 (2017).
- 15 Ge, Q. *et al.* Multimaterial 4D printing with tailorable shape memory polymers. *Sci. Rep.* **6**, 31110 (2016).
- 16 Zhang, B. *et al.* Self-Healing Four-Dimensional Printing with an Ultraviolet Curable Double-Network Shape Memory Polymer System. *ACS Appl. Mater. Interfaces* **11**, 10328-10336 (2019).
- 17 Zhao, T. *et al.* 4D printing of shape memory polyurethane via stereolithography. *Eur. Polym. J.* **101**, 120-126 (2018).
- 18 Choong, Y. Y. C., Maleksaeedi, S., Eng, H., Wei, J. & Su, P.-C. 4D printing of high performance shape memory polymer using stereolithography. *Mater. Des.* **126**, 219-225 (2017).
- 19 Zhang, B. *et al.* Highly stretchable hydrogels for UV curing based high-resolution multimaterial 3D printing. *J. Mater. Chem. B.* **6**, 3246-3253 (2018).
- 20 Xu, T. *et al.* Structural colors: from plasmonic to carbon nanostructures. *Small* **7**, 3128-3136 (2011).
- 21 Gu, Y., Zhang, L., Yang, J. K., Yeo, S. P. & Qiu, C.-W. Color generation via subwavelength plasmonic nanostructures. *Nanoscale* **7**, 6409-6419 (2015).
- 22 Laux, E., Genet, C., Skauli, T. & Ebbesen, T. W. Plasmonic photon sorters for spectral and polarimetric imaging. *Nat. Photonics* **2**, 161 (2008).
- 23 Duempelmann, L., Luu-Dinh, A. I., Gallinet, B. & Novotny, L. Four-fold color filter based on plasmonic phase retarder. *ACS Photonics* **3**, 190-196 (2015).
- 24 Chung, K. *et al.* Flexible, angle-independent, structural color reflectors inspired by morpho butterfly wings. *Adv. Mater.* **24**, 2375-2379 (2012).
- 25 Kats, M. A., Blanchard, R., Genevet, P. & Capasso, F. Nanometre optical coatings based on strong interference effects in highly absorbing media. *Nat. Mater* **12**, 20 (2013).
- 26 Zhao, Q., Zhou, J., Zhang, F. & Lippens, D. Mie resonance-based dielectric metamaterials. *Mater. Today* **12**, 60-69 (2009).
- 27 Kumar, K. *et al.* Printing colour at the optical diffraction limit. *Nat. Nanotechnol.* **7**, 557 (2012).

- 28 Cetin, A. E., Mertiri, A., Huang, M., Erramilli, S. & Altug, H. Thermal tuning of surface plasmon polaritons using liquid crystals. *Adv. Opt. Mater.* **1**, 915-920 (2013).
- 29 Dong, W. *et al.* Wide bandgap phase change material tuned visible photonics. *Adv. Funct. Mater.* **29**, 1806181 (2019).
- 30 Franklin, D. *et al.* Polarization-independent actively tunable colour generation on imprinted plasmonic surfaces. *Nat. Commun.* **6**, 1-8 (2015).
- 31 Millyard, M. G. *et al.* Stretch-induced plasmonic anisotropy of self-assembled gold nanoparticle mats. *Appl. Phys. Lett.* **100**, 073101 (2012).
- 32 Cataldi, U. *et al.* Growing gold nanoparticles on a flexible substrate to enable simple mechanical control of their plasmonic coupling. *J. Mater. Chem. C* **2**, 7927-7933 (2014).
- 33 Yu, K., Ge, Q. & Qi, H. J. Reduced time as a unified parameter determining fixity and free recovery of shape memory polymers. *Nat. Commun.* **5**, 1-9 (2014).
- 34 Jang, J.-H., Koh, C. Y., Bertoldi, K., Boyce, M. C. & Thomas, E. L. Combining pattern instability and shape-memory hysteresis for phononic switching. *Nano Lett.* **9**, 2113-2119 (2009).
- 35 Wang, Z. *et al.* Programmable, pattern-memorizing polymer surface. *Adv. Mater.* **23**, 3669-3673 (2011).
- 36 Xu, H. *et al.* Deformable, programmable, and shape-memorizing micro-optics. *Adv. Funct. Mater.* **23**, 3299-3306 (2013).
- 37 Fang, Y. *et al.* Reconfigurable photonic crystals enabled by pressure-responsive shape-memory polymers. *Nat. Commun.* **6**, 7416 (2015).
- 38 Fang, Y. *et al.* Reconfigurable photonic crystals enabled by multistimuli-responsive shape memory polymers possessing room temperature shape processability. *ACS Appl. Mater. Interfaces* **9**, 5457-5467 (2017).
- 39 Ding, T. *et al.* Revealing invisible photonic inscriptions: images from strain. *ACS Appl. Mater. Interfaces* **7**, 13497-13502 (2015).
- 40 Liu, Y. *et al.* Structural color three-dimensional printing by shrinking photonic crystals. *Nat. Commun.* **10**, 1-8 (2019).
- 41 Zeng, H. *et al.* High-resolution 3D direct laser writing for liquid-crystalline elastomer microstructures. *Adv. Mater.* **26**, 2319-2322 (2014).
- 42 Wang, H., Wang, H., Zhang, W. & Yang, J. K. Towards Near-Perfect Diffractive Optical Elements via Nanoscale 3D Printing. *ACS Nano* (2020).
- 43 Wang, S. *et al.* Sub-10-nm suspended nano-web formation by direct laser writing. *Nano Futures* **2**, 025006 (2018).
- 44 Nishiguchi, A. *et al.* 4D Printing of a Light-Driven Soft Actuator with Programmed Printing Density. *ACS Appl. Mater. Interfaces* **12**, 12176-12185 (2020).
- 45 Zeng, H. *et al.* Light-fueled microscopic walkers. *Adv. Mater.* **27**, 3883-3887 (2015).
- 46 Bozuyuk, U. *et al.* Light-triggered drug release from 3D-printed magnetic chitosan microswimmers. *ACS Nano* **12**, 9617-9625 (2018).
- 47 Wang, X. *et al.* MOFBOTS: Metal-Organic-Framework-Based Biomedical Microrobots. *Adv. Mater.* **31**, 1901592 (2019).
- 48 Xia, X. *et al.* Electrochemically reconfigurable architected materials. *Nature* **573**, 205-213 (2019).
- 49 Spiegel, C. A. *et al.* 4D Printing at the Microscale. *Adv. Funct. Mater.*, 1907615 (2019).
- 50 Del Pozo, M. *et al.* Direct Laser Writing of Four-Dimensional Structural Color Microactuators Using a Photonic Photoresist. *ACS Nano* (2020).
- 51 Tao, Y., Xiong, W., Deng, C., Liu, J. & Lu, C. Bio-mimic four-dimensional printing of nanostructured interactive hydrogels. Preprint at <https://arxiv.org/abs/2006.04019> (2020).
- 52 Wang, H. *et al.* Off-Axis Holography with Uniform Illumination via 3D Printed Diffractive Optical Elements. *Adv. Opt. Mater.* **7**, 1900068 (2019).
- 53 Chan, J. Y. E., Ruan, Q., Ng, R. J. H., Qiu, C.-W. & Yang, J. K. Rotation-Selective Moiré Magnification of Structural Color Pattern Arrays. *ACS Nano* **13**, 14138-14144 (2019).
- 54 Lim, K. T., Liu, H., Liu, Y. & Yang, J. K. Holographic colour prints for enhanced optical security by combined phase and amplitude control. *Nat. Commun.* **10**, 25 (2019).

- 55 Duan, H., Yang, J. K. & Berggren, K. K. Controlled Collapse of High - Aspect - Ratio Nanostructures. *Small* **7**, 2661-2668 (2011).
- 56 Seniutinas, G. *et al.* Beyond 100 nm resolution in 3D laser lithography—Post processing solutions. *Microelectron. Eng.* **191**, 25-31 (2018).
- 57 Urbancová, P. *et al.* IP-Dip-based woodpile structures for VIS and NIR spectral range: complex PBG analysis. *Opt. Mater. Express* **9**, 4307-4317 (2019).

Supplementary Information

Structural Multi-Colour Invisible Inks with Submicron 4D Printing of Shape Memory Polymers

Wang Zhang¹, Hao Wang^{1*}, Hongtao Wang¹, John You En Chan¹, Hailong Liu^{1,2}, Biao Zhang³, Yuan-Fang Zhang⁴, Komal Agarwal¹, Xiaolong Yang⁵, Hong Yee Low¹, Qi Ge⁶, Joel K.W. Yang^{1,2*}

¹Engineering Product Development, Singapore University of Technology and Design, Singapore 487372, Singapore. ²Nanofabrication Department, Institute of Materials Research and Engineering, Singapore 138634, Singapore. ³Frontiers Science Center for Flexible Electronics, Xi'an Institute of Flexible Electronics (IFE) and Xi'an Institute of Biomedical Materials & Engineering (IBME), Northwestern Polytechnical University, 127 West Youyi Road, Xi'an 710072, China. ⁴Digital Manufacturing and Design Centre, Singapore University of Technology and Design, Singapore 487372, Singapore. ⁵National Key Laboratory of Science and Technology on Helicopter Transmission, Nanjing University of Aeronautics and Astronautics, Nanjing 210016, China. ⁶Department of Mechanical and Energy Engineering, Southern University of Science and Technology, Shenzhen 518055, China.

*email: hao_wang@sutd.edu.sg; joel_yang@sutd.edu.sg

1. Chemical compositions of the photoresist

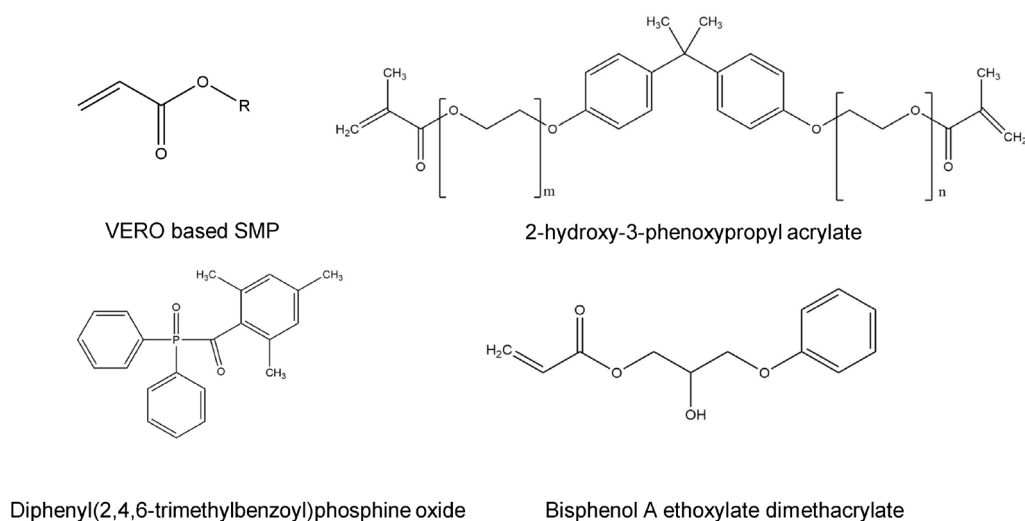


Figure S1. Chemical structures of the components in the customized photoresist

2. Materials characterization

To develop a suitable resist for additive manufacturing of shape memory polymer, one needs to satisfy several criteria simultaneously: (1) sufficient viscosity for patterning with our TPL system, (2) a suitable T_g , e.g., above room temperature, and (3) sufficient deformability to avoid irreversible damage during the programming process as described in Figure 1. To meet these demands, we cured macroscopic films (0.5mm thick) of the resist in ultraviolet light to perform mechanical tests. Results are shown in Figure S2a-d. As the temperature increases, the storage modulus decreases for all concentrations due to the viscoelasticity of the SMP (Figure S2a). At the same temperature, the storage modulus decreases as the increase of the concentration of the elastomer, which has a much smaller elasticity modulus than Vero Clear. Figure S2b plots $\tan \delta$, i.e. the ratio of loss modulus (corresponding to energy dissipation) and storage modulus, as a function of temperature. The peaks of these plots correspond to the glass transition temperature of the particular composition of Vero Clear to elastomer ratio. A single $\tan \delta$ peak indicates that the blend of elastomer and Vero Clear co-cured without phase separation. The T_g for pure Vero Clear is $\sim 65^\circ\text{C}$ and $\sim 17^\circ\text{C}$ for pure elastomer. As the concentration of the elastomer increases from 10% to 50%, T_g decreases from 54°C to 29°C . Varying the ratio of Vero Clear to elastomer thus allows for prints that respond to a range of temperatures. For convenience, we chose a T_g of $\sim 40^\circ\text{C}$, i.e. above room temperature for the programmed structures to be maintainable without external load at room temperature.

Figure S2c presents the stress-strain curves of the polymer blends above T_g . The temperature was set to 20 °C above the corresponding T_g for each composition. As the blend of Vero Clear and the elastomers is homogenous as shown by the tan delta results, expectedly, the strain at failure increases from 34% to 85% (Figure S2c inset) with increasing elastomer content. For the interest of this study, the mass ratio of 7:3 of Vero Clear and elastomer was chosen which has a strain at failure of ~50%. It should be noted that the mechanical tests in Figure S2a-c were conducted by UV cured macroscopic films of 0.5 mm and the patterned film by the TPL process is in the submicrometer range. The mechanical properties of TPL patterned structures are likely to be similar to that of the bulk film.

In the Dip-in Laser Lithography (DiLL) configuration of Nanoscribe, the viscosity of the photoresist should be controlled: A viscosity that is too low would result in the resist flowing away (unless gaskets are used) as the sample stage moves during printing. A viscosity that is too high could reduce the print resolution by suppressing the diffusion of oxygen inside the resist, which acts as quencher of the photopolymerization process¹. The developed SMP photoresists in our work have viscosities between 140 to 220 mPa·s (as shown in Figure S2d), which is about 10 times less viscous than the commercial photoresist IP-Dip (2420 mPa·s according to the official datasheet). Nonetheless, we were able to expose and pattern high resolution structures without problem, indicating a suitable viscosity range of the resist within the TPL system.

To examine the resolution of this resist, we exposed a series of single-pixel lines on a base layer (~2µm thick), used to aid adhesion. Figures S2e-f show scanning electron micrographs (SEM) of patterns formed in a resist with a 7:3 mass ratio composition of Vero Clear to elastomer. The linewidth decreases as expected with decreasing laser power and increasing write speed (Figure S2e). The polymerization threshold of 30 mW was determined at a reasonable write speed of ~1.1mm/s resulting in a linewidth of ~280 nm. This write speed is an order of magnitude slower than that for the commercial TPL photoresist IP-Dip², which may be attributed to lower reaction speeds of both the initiator and monomer. Though the linewidth can be further reduced by lowering the laser power, the resultant structures tend to collapse due to poor mechanical strength³. Hence, the lowest laser power used in this work was 30 mW. To determine the resolution limit, we fabricated lines with different pitches with a fixed write speed of 1.1mm/s while varying the laser power, as shown in Figure S2f. A conservative minimum resolvable pitch was determined to be 600 nm (i.e. 300 nm half pitch). Gaps between lines at 400 nm pitch were not well defined.

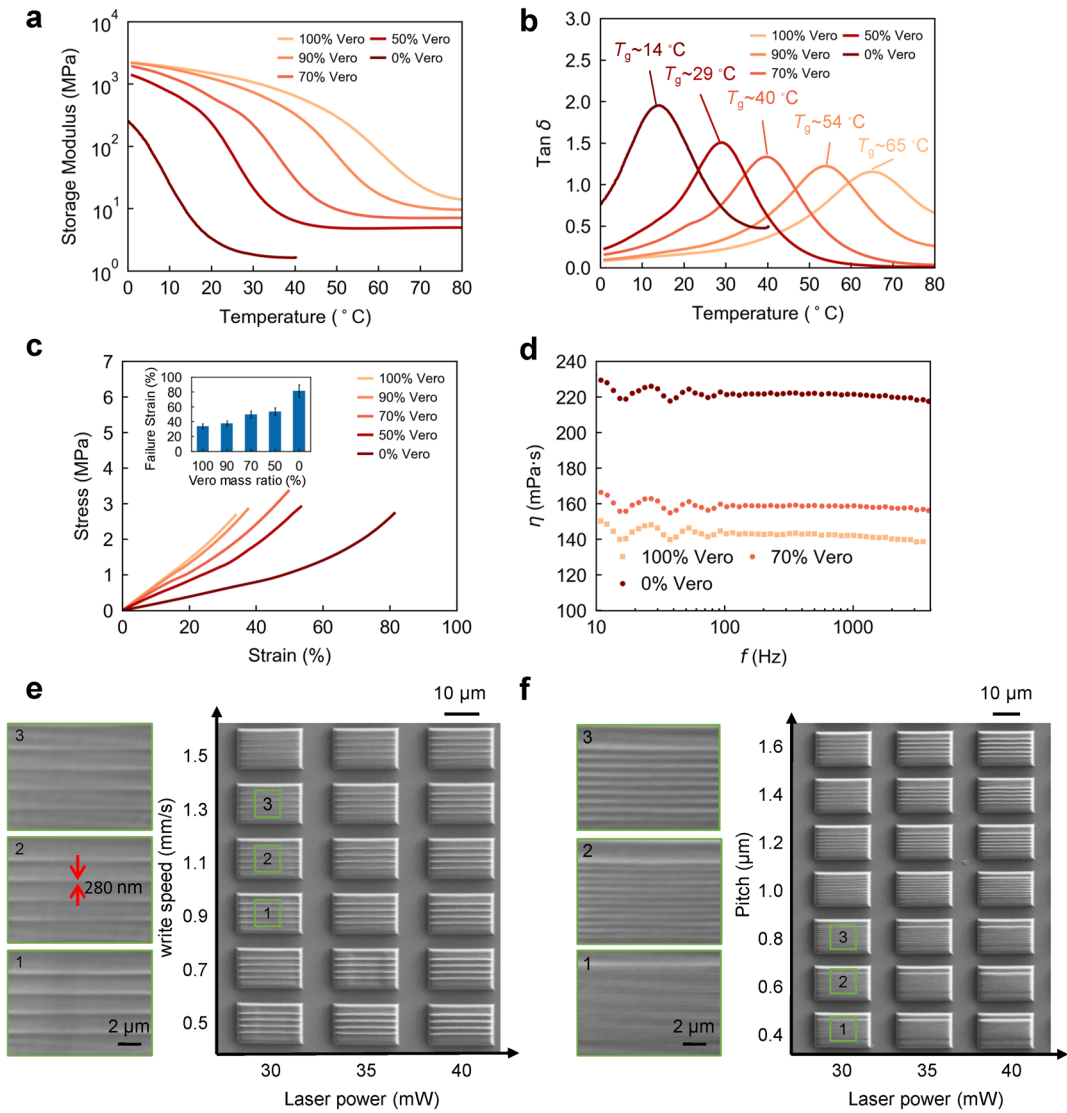


Figure S2. Mechanical characterization for different mass ratios of Vero Clear to elastomer in the photoresist. (a) Storage modulus as a function of temperature; (b) Plot of $\tan \delta$ values versus temperature; (c) Uniaxial tensile tests at high temperature at 20 °C above the glass transition temperature (T_g) (inset) Failure strain at different Vero Clear mass ratios; (d) Photoresist viscosity tests for pure Vero Clear, pure elastomer and 70% Vero Clear, respectively; (e) Left: High-magnification Scanning Electron Micrographs (SEM) of single-pixel lines fabricated with laser power of 30mW and write speed of 0.9mm/s, 1.1 mm/s and 1.3 mm/s respectively; Right: SEM images of lines fabricated at different laser powers and write speeds to determine crosslinking threshold; (f) Left: High-magnification SEM images of lines fabricated with laser power of 30 mW, write speed of 1.1 mm/s and pitches 0.4 μm , 0.6 μm and 0.8 μm respectively; Right: SEM images of lines fabricated with a fixed write speed of 1.1mm/s and different laser powers to determine print resolution.

3. Fabrication parameters

Different structures in the manuscript were fabricated with different parameters. See Table S1 for the fabrication parameters.

Table S1. Fabrication parameters*

Figures	Laser power (mW)	Writing speed (mm/s)	Pitching (μm)	Hatching (μm)	Number of grid layers
Figure S2e (Bottom surface)	35	2	0.2	0.4	5
Figure S2e (Up grids)	30-45	0.5-1.5	2	0.3	1
Figure S2f (Bottom surface)	35	2	0.2	0.4	5
Figure S2f (Up grids)	30-45	1.1	0.4-2	0.3	1
Figure 2a (Bottom surface)	35	2	0.2	0.4	10
Figure 2a (Up grids)	30-35	0.5-1.4	2	0.3	5-10
Figure S4 (Bottom surface)	35	2	0.2	0.4	10
Figure S4 (Up grids)	30	0.6	2	0.3	7
Figure 4a (Bottom surface)	35	2	0.2	0.4	10
Figure 4a (Up grids)	30	0.6-1.1	2	0.3	7
Figure 4d-f (Bottom surface)	35	2	0.2	0.4	10
Figure 4d-f (Up grids)	32.5	0.8	2	0.3	7
Figure 4g (Bottom surface)	35	2	0.2	0.4	10
Figure 4g (Up grids)	30	0.5-1.2	2	0.3	4-9

(*The first layer of grids was printed at the same vertical coordinate as the last layer of the base surface to increase bonding between the grids and the base surface)

4. Calculated colour coordinates of Figure 3aI in the CIE 1931 chromaticity diagram

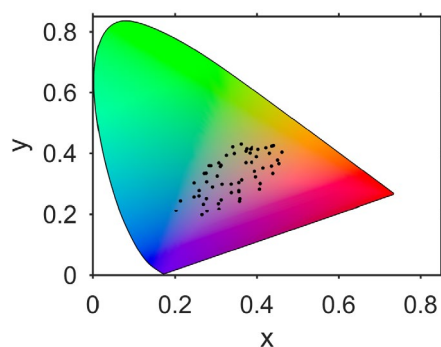


Figure S3. Calculated colour coordinates of Figure 3aI mapped onto the CIE 1931 chromaticity diagram, providing an indication of the gamut achieved from the grid structures;

5. Effect of pitch w_2 on the spectra

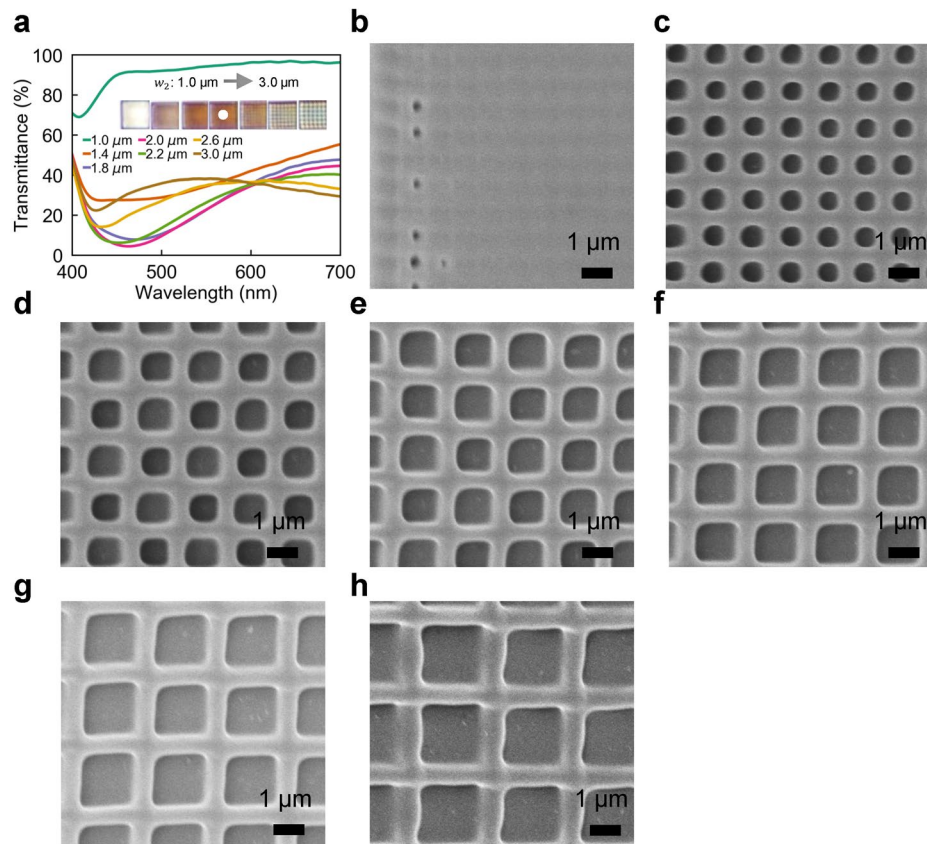


Figure S4. (a) A comparison of transmittance spectra for different pitches w_2 ; (b)-(h) SEM images of grid structures with pitches of 1 μm , 1.4 μm , 1.8 μm , 2.0 μm , 2.2 μm , 2.6 μm , 3.0 μm , respectively.

6. SEM images of grid structures fabricated with different laser power

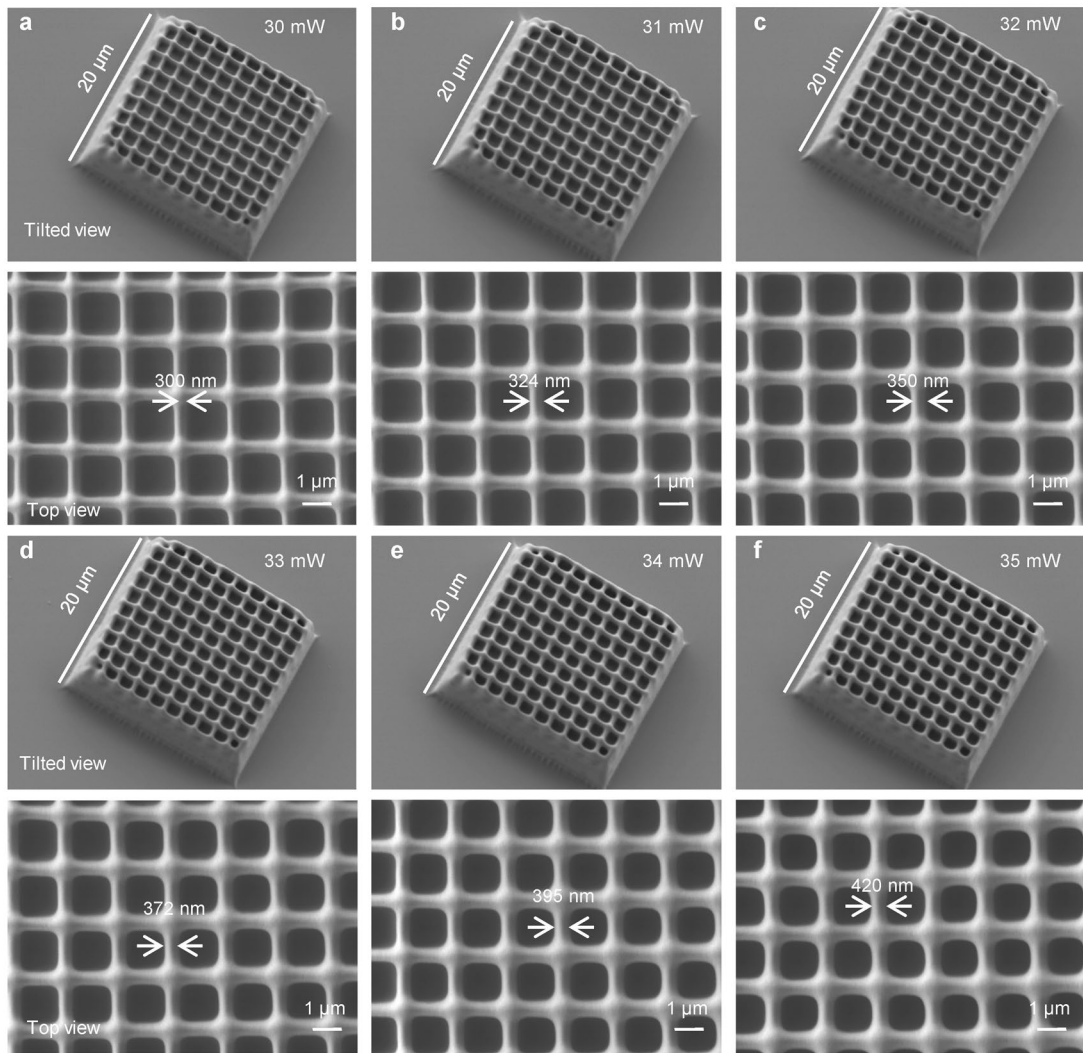


Figure S5. SEM images of grid structures fabricated with fixed write 1mm/s and nominal height $w_2=1.8 \mu\text{m}$ while varying the laser power from 30 mW to 35 mW.

7. Determining of the refractive index used in the FDTD simulation

To measure the refractive index of the photoresist, a wafer substrate was first washed by IPA and then baked on a hotplate at 130 °C for 10 mins. Then the resist was spin coated on the substrate with a speed of 7000 rpm for 1 min. Then the substrate was baked again on the hotplate 130 °C for 3 mins.

The ellipsometry angles Δ and Ψ were measured by an EP4 ellipsometer (ACCURION, Germany). The measured data were fitted by the Cauchy dispersion function as shown in Eq. (S1) and Eq. (S2), where A , B , C , A_1 , B_1 , C_1 are parameters for the Cauchy dispersion which can be determined by fitting the measured ellipsometric angles Δ and Ψ . n and k are refractive

index and extinction coefficient of the material, respectively. The fitting process was done by the Levenberg-Marquardt algorithm in the EP4 model software.

$$n(\lambda) = A + \frac{B}{\lambda^2} + \frac{C}{\lambda^4} \quad (\text{S1})$$

$$k(\lambda) = A_1 + \frac{B_1}{\lambda^2} + \frac{C_1}{\lambda^4} \quad (\text{S2})$$

The fitted parameters are given in Table S2

Table S2 Cauchy dispersion parameters for the photoresist

A	B	C	A_1	B_1	C_1
1.489	2998	4.317*e8	0	0	0

After fitting the dispersion function, the refractive index n and k as functions of wavelength are obtained and plotted in Figure S6.

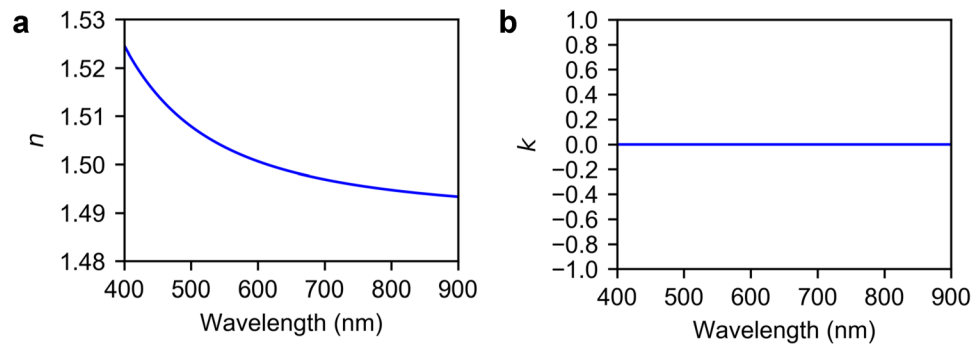


Figure S6 Determining of the refractive index (a) Fitted refractive index n ; (b) Fitted extinction coefficient k .

8. A comparison of the measured and simulated spectra

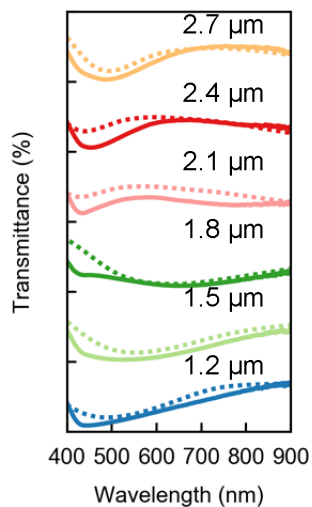


Figure S7. A comparison of the measured and simulated spectra

9. Relation between line width w_1 and dip position

As the increase of line width w_1 , the effective index $R_e = \sqrt{\varepsilon_e}$ increases because the volume fraction of the polymer to air increases. The effective permittivity ε_e can be calculated by the modified Maxwell Garnett effective medium model⁴,

$$\varepsilon_e = \varepsilon_a \frac{\varepsilon_p (1 + 2f) + \varepsilon_a (2 - 2f)}{\varepsilon_p (1 - f) + \varepsilon_a (2 + f)} \quad (\text{S3})$$

where ε_p and ε_a are the permittivities of polymer and air respectively. $\varepsilon_p = n_p^2$ and $\varepsilon_a = n_a^2$, where n_p and n_a are the refractive indexes of polymer and air, respectively. n_p can be obtained by the fitted data in Figure S6a, and $n_a = 1.003$. The volume fraction of polymer can be calculated using

the geometry relation as shown in Figure S8a, and $f = \frac{w_2^2 - (w_2 - w_1)^2}{w_2^2}$. The dip position λ can

be obtained from the simulated data in Figure 3f. Using the above data and formulas, the dip position and effective index as functions of line width can be obtained by the Least square polynomial fit as shown in Figure S8b. Both λ and n_e show strong linear relation with w_1 , from which we can derive a linear relation between λ and n_e as $\lambda = 1500n_e - 1210.5$. This relation is analogous to the relation between λ and n in diffraction grating formula $\lambda = \frac{dn \sin \theta_m}{m} + C$,

where d is the grating period, θ_m is the angle between the diffracted ray and the grating's normal vector, C is a constant to be fitted.

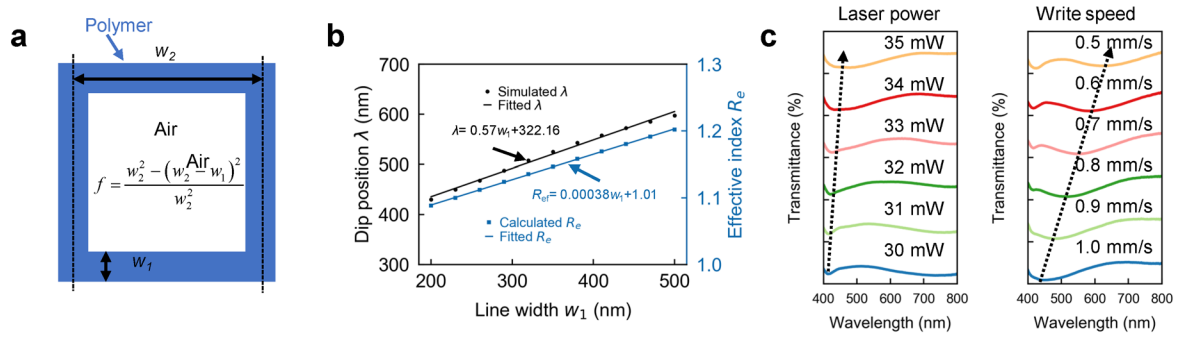


Figure S8. (a) Determining of polymer volume fraction; (b) Dip position and effective index as functions of linewidth; (c) Measured spectra with the variation of fabricating laser power and write speed. (Left spectra were measured from structures in Figure 2a with fixed write speed of 1 mm/s, nominal height h_2 of 1.8 μm ; Right spectra were measured from structures in Figure 2a with fixed laser power of 30 mW, nominal height of 2.7 μm).

10. The programming progress

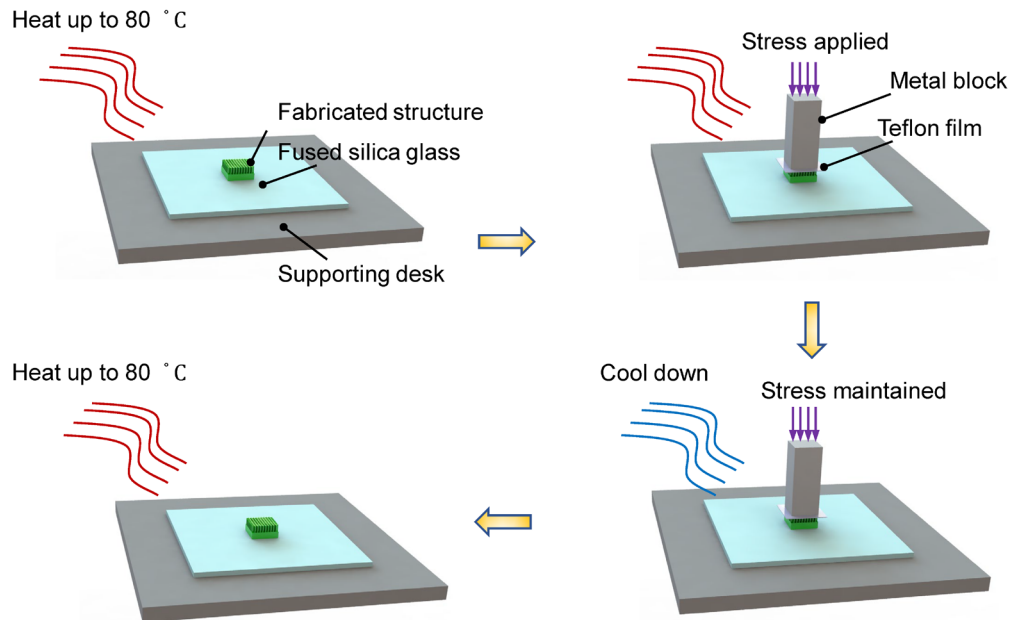


Figure S9. Schematic of the 4D programming process. The structure was first heat up to 80 °C by a heat gun. The temperature was monitored by a thermometer. Then a stress of $\sim 500\text{kPa}^*$ was applied through a metal block. A layer of Teflon film was put between the structure and the block to avoid contamination. The heat gun was removed afterward, and the structure was cooled down to room temperature with the stress maintained. Finally, the stress was removed, and the structure was heat up to 80 °C to recover. (*The stress was estimated by the following process: A force applied by thumb was estimated to be $\sim 50\text{ N}$ based on Ref.⁵; The contact area of the metal surface and the support was $1\text{cm} \times 1\text{cm}$; The pressure $P \approx \frac{50\text{N}}{1\text{cm} \times 1\text{cm}} = 500\text{kPa}$)

11. SEM images of the painting

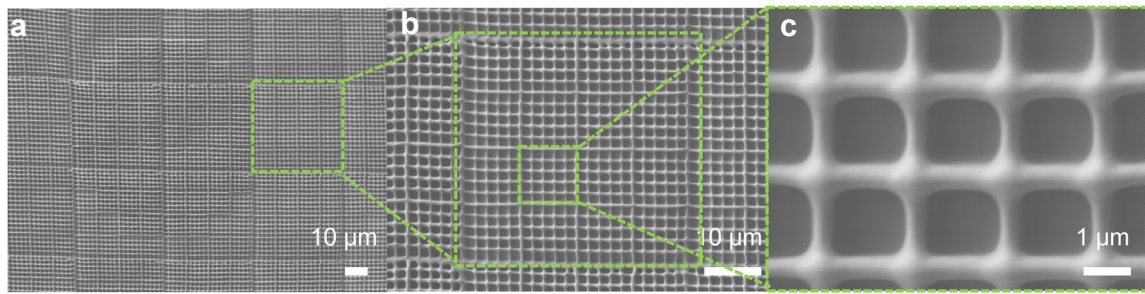


Figure S10. (a)-(c) SEM images of the painting

Supplementary References

- 1 Zandrini, T. *et al.* Effect of the resin viscosity on the writing properties of two-photon polymerization. *Opt. Mater. Express* **9**, 2601-2616 (2019).
- 2 Urbancová, P. *et al.* IP-Dip-based woodpile structures for VIS and NIR spectral range: complex PBG analysis. *Opt. Mater. Express* **9**, 4307-4317 (2019).
- 3 Lemma, E. D. *et al.* Mechanical properties tunability of three-dimensional polymeric structures in two-photon lithography. *IEEE Trans. Nanotechnol.* **16**, 23-31 (2016).
- 4 Frame, J. D., Green, N. G. & Fang, X. Modified Maxwell Garnett model for hysteresis in phase change materials. *Opt. Mater. Express* **8**, 1988-1996 (2018).
- 5 Radwin, R. G., Oh, S., Jensen, T. R. & Webster, J. G. External finger forces in submaximal five-finger static pinch prehension. *Ergonomics* **35**, 275-288 (1992).